Noname manuscript No.
(will be inserted by the editor)

An International Standard Formulation for 2,3,3,3-Tetrafluoroprop-1-ene (R1234yf) Covering Temperatures from the Triple-point Temperature to 410 K and Pressures up to 100 MPa

Eric W. Lemmon · Ryo Akasaka

Received: date / Accepted: date

Abstract A new fundamental equation of state is presented for 2,3,3,3-tetrafluoroprop-1-ene (R1234yf). The equation is valid from the triple point temperature (121.6 K) to 410 K at pressures up to 100 MPa, where typical expanded uncer-

Eric W. Lemmon

Applied Chemicals and Materials Division, National Institute of Standards and Technology, Boulder, CO 80305, USA

E-mail: eric.lemmon@nist.gov

ORCID: 0000-0002-0974-0203

Ryo Akasaka

Department of Mechanical Engineering, Faculty of Science and Engineering, Kyushu Sangyo University, Fukuoka 8138503, Japan

Research Center for Next Generation Refrigerant Properties (NEXT-RP), International Institute for Carbon-Neutral Energy Research (WPI-I2CNER), Kyushu University, Fukuoka 8190395, Japan

E-mail: ryo-a@ip.kyusan-u.ac.jp

ORCID: 0000-0003-2641-6031

tainties ($k = 2$) in calculated properties from the equation are 0.1 % for vapor pressures at temperatures above 270 K and 0.3 % at lower temperatures, 0.1 % for liquid densities at pressures below 40 MPa and 0.25 % at higher pressures, 0.2 % for vapor densities, 0.02 % for vapor-phase sound speeds, 0.05 % for liquid-phase sound speeds, 1 % for vapor-phase isobaric heat capacities, 2 % for liquid-phase isobaric heat capacities, and 2 % for liquid-phase isochoric heat capacities. At very low temperatures around 200 K, uncertainties for vapor pressures may be larger than 0.5 %. Various plots of constant-property lines demonstrate that not only does the equation exhibit correct behavior over all temperatures and pressures within the range of validity, but also that it shows reasonable extrapolation behavior at extremely low and high temperatures, and at high pressures and densities. The equation of state is the best currently available property representation for R1234yf, and has been adopted as an international standard by the ISO working group, which recently revised ISO/DIS 17584 (Refrigerant properties).

Keywords R1234yf · Equation of state · Vapor pressure · Density · Heat capacity · Sound speed

1 Introduction

2,3,3,3-Tetrafluoroprop-1-ene (CAS 754-12-1), also known as R1234yf, is the most studied and widely used hydrofluoroolefin (HFO) refrigerant, with a low global warming potential (GWP); IPCC AR5 [1] reported that the 100-yr GWP of R1234yf is less than 1. This comes from the short atmospheric lifetime

of 11 days [2] due to the carbon-carbon double bond. It is a stable and low-toxicity fluid under normal conditions, but it is mildly flammable and has been assigned a safety classification of A2L according to ASHRAE Standard 34 [3].

The refrigeration industry considers this novel compound a core refrigerant for next-generation air conditioning and cooling systems. R1234yf was initially given attention as a possible alternative to 1,1,1,2-tetrafluoroethane (R134a) as a refrigerant for mobile air conditioners. Nowadays, automotive air conditioners are dominated by systems containing R1234yf. Furthermore, R1234yf is an important constituent in low-GWP refrigerant mixtures. Refrigerant blends proposed for residential air conditioners over the last decade often include more than 30 mass% of R1234yf.

The first fundamental equation of state for R1234yf was developed by Richter et al. [4] in 2011. Akasaka [5] presented a different equation of state in the same year. Although these equations were based on limited experimental data, they represented the vapor pressures, densities, and heat capacities with sufficient accuracies. The equation by Richter et al. [4] has often been applied to various studies on thermodynamic properties, heat transfer characteristics, refrigeration cycle analysis, and drop-in tests and has greatly contributed to realizing practical use of R1234yf.

After the first equations were published, as high-purity samples of R1234yf became available, additional measurements were reported for vapor pressures, (p, ρ, T) data at high pressures, isobaric heat capacities, isochoric heat capacities, and sound speeds. The amount of these new data is sufficient to update

the equation. This work presents a new fundamental equation of state for R1234yf. All experimental data currently available were evaluated in terms of uncertainties and thermodynamic consistency; only selected data were employed while fitting the equation of state. The final equation presented here has been adopted as an international standard by the ISO working group, which recently revised ISO/DIS 17584 (Refrigerant properties) [6].

2 Fundamental Constants

Table 1 lists the fixed-point constants of R1234yf. All properties are calculated from the equation of state of this work, except the molar mass M, universal gas constant R, critical temperature T_{c}, and triple-point temperature T_{tp}. Accurate values for the critical parameters, particularly the critical temperature, are necessary to formulate reliable equations of state since they are always used as the reducing parameters for the independent variables. Tanaka and Higashi [7] determined experimentally the critical temperature and density of R1234yf; they are 367.85 ± 0.01 K and 478 ± 3 kg $\cdot$ m^{-3} (≈ 4.191 mol $\cdot$ dm^{-3}), respectively. This critical temperature was used here as the reducing temperature for the equation of state. Experimental critical densities generally involve larger uncertainties than those in critical temperatures due to the infinite compressibility at the critical point and the difficulty of reaching thermodynamic equilibrium; this work used the critical density of Tanaka and Higashi [7] as an initial value for the reducing density, which was then slightly adjusted during the fitting of the equation of state. This yielded better representa-

tions of densities and vapor pressures in the critical region. The final value for the critical density is 4.18 $\mathrm{mol \cdot dm^{-3}}$, which is within the experimental uncertainty. Tanaka and Higashi [7] also determined the critical pressure as 3.382 ± 0.003 MPa by extrapolating the vapor pressure curve to the critical point. The equation of state calculates the critical pressure as 3.3844 MPa at 367.85 K and 4.18 $\mathrm{mol \cdot dm^{-3}}$. Di Nicola et al. [8] reported the triple point of R1234yf as 122.6 K with an uncertainty of ±0.8 K. Tomassetti et al. [9] recently measured the triple-point temperature with two different apparatus; their measurements are 121.6 ± 0.5 K and 121.8 ± 1.0 K. Because of its lower uncertainty, this work adopted the value of Tomassetti et al. [9] (121.6 K) as the triple-point temperature, which is also used as the lower temperature limit for the applicable range of the equation of state. The vapor pressure at the triple point is calculated as 0.4127 Pa with the final equation of state.

3 Ancillary Equations

Ancillary equations for the vapor pressure and saturated liquid and vapor densities were formulated based on calculated values from the equation of state. They provide rapid calculations of the saturation properties and also give excellent initial guesses for the iterative process to find rigorous solutions from the equation of state based on the Maxwell criterion. The ancillary equations presented here fulfill the requirements stated by Lemmon and Goodwin [10] for vapor pressure correlations and Gao et al. [11] for saturated liquid and

Table 1 Fixed-point constants and other characteristic properties of R1234yf[a].

Property	Symbol	Unit	Value
CAS number			754-12-1
Chemical formula			$CF_3CF{=}CH_2$
Molar mass	M	$\mathrm{g \cdot mol^{-1}}$	114.0416
Molar gas constant	R	$\mathrm{J \cdot mol^{-1} \cdot K^{-1}}$	8.314462618
Critical temperature	T_c	K	367.85
Critical pressure	p_c	MPa	3.3844
Critical density	ρ_c	$\mathrm{mol \cdot dm^{-3}}$	4.18
Triple-point temperature	T_tp	K	121.6
Triple-point pressure	p_tp	Pa	0.4127
Saturated liquid density at triple point	ρ'_tp	$\mathrm{mol \cdot dm^{-3}}$	13.836
Saturated vapor density at triple point	ρ''_tp	$\mathrm{mol \cdot dm^{-3}}$	4.082×10^{-7}
Normal boiling point temperature	T_b	K	243.692
Saturated liquid density at normal boiling point	ρ'_b	$\mathrm{mol \cdot dm^{-3}}$	11.076
Saturated vapor density at normal boiling point	ρ''_b	$\mathrm{mol \cdot dm^{-3}}$	0.05240
Reference temperature for ideal gas properties	T_0	K	273.15
Reference pressure for ideal gas properties	p_0	MPa	0.001
Reference ideal-gas enthalpy at T_0	h°_0	$\mathrm{J \cdot mol^{-1}}$	42251.66738496
Reference ideal-gas entropy at T_0 and p_0	s°_0	$\mathrm{J \cdot mol^{-1} \cdot K^{-1}}$	232.28205919
Acentric factor	ω	–	0.276

[a]All properties in this table were determined in this work except M, R, T_c, and T_tp.

vapor densities correlations. The coefficients N_i of each equation are given in Table 2.

The equation for the vapor pressure p_s is

$$\ln\left(\frac{p_\mathrm{s}}{p_\mathrm{c}}\right) = \frac{T_\mathrm{c}}{T}\left(N_1\theta + N_2\theta^{1.5} + N_3\theta^2 + N_4\theta^4 + N_5\theta^9\right), \tag{1}$$

where p_c is the critical pressure (3.3844 MPa), T_c is the critical temperature (367.85 K), and $\theta = 1 - T/T_\mathrm{c}$. Equation 1 is valid at temperatures from the triple point (121.6 K) to the critical temperature, with an average relative deviation of 0.014 % from the rigorous Maxwell solution. The saturated liquid and vapor densities (ρ' and ρ'') are calculated from the equations

$$\frac{\rho'}{\rho_\mathrm{c}} = 1 + N_1\theta^{0.4} + N_2\theta^{0.7} + N_3\theta^{1.1} + N_4\theta^{1.5} + N_5\theta^{2.1} \tag{2}$$

and

$$\ln\left(\frac{\rho''}{\rho_\mathrm{c}}\right) = N_1\theta^{0.426} + N_2\theta^2 + N_3\theta^{2.4} + N_4\theta^{2.7} + N_5\theta^{7.5} + N_6\theta^{15}, \tag{3}$$

where ρ_c is the critical density (4.18 $\mathrm{mol}\cdot\mathrm{dm}^{-3}$). Equations 2 and 3 are applicable in the range from the triple-point temperature to the critical temperature, with average relative deviations from the rigorous Maxwell solution of 0.022 % in Eq. 2 and 0.040 % in Eq. 3. Deviations of up to 0.2 % are sometimes observed from Eq. 3 at temperatures above $0.98T_\mathrm{c}$.

4 Equation of State

The equation of state is expressed explicitly in the Helmholtz energy as the fundamental property with independent variables of temperature and density.

Table 2 Coefficients of Eqs. 1, 2, and 3.

	Eq. 1	Eq. 2	Eq. 3
N_1	−7.4507	3.392	−3.616
N_2	2.164	−4.119	−74.91
N_3	−1.674	8.932	197.7
N_4	−3.318	−8.525	−152.76
N_5	−1.617	3.384	−61.062
N_6			−115.53

The equation has the form

$$\frac{a(T,\rho)}{RT} = \alpha(\tau,\delta) = \alpha^{\circ}(\tau,\delta) + \alpha^{\mathrm{r}}(\tau,\delta), \tag{4}$$

where a is the molar Helmholtz energy, α is the dimensionless Helmholtz energy, $R = 8.314462618\ \mathrm{J \cdot mol^{-1} \cdot K^{-1}}$ is the molar gas constant, $\tau = T_{\mathrm{c}}/T$ is the reciprocal reduced temperature, and $\delta = \rho/\rho_{\mathrm{c}}$ is the reduced density. The value of R is a slightly rounded value of the exact value [12]. The dimensionless Helmholtz energy α is split into an ideal-gas part α° representing ideal-gas properties and a residual part α^{r} corresponding to the influence of intermolecular forces between molecules.

The Helmholtz energy given by Eq. 4 is one of four fundamental functions in thermodynamics, where all thermodynamic properties in single phase states can be calculated from its derivatives with respect to temperature and density. Mathematical expressions for calculating thermodynamic properties from the Helmholtz energy are presented in the literature, e.g., Span [13] and Lemmon and Jacobsen [14]. The location of the saturation boundaries requires an iter-

ative solution of the physical constraints on saturation (the Maxwell criteria). Kretzschmar et al. [15], Span [13], and Akasaka [16] discuss robust numerical algorithms to correctly obtain the Maxwell solutions.

4.1 Ideal-gas Helmholtz Energy

The ideal-gas Helmholtz energy α° is analytically derived from an equation for the isobaric heat capacity of the ideal gas (c_p°). The following equation gives the ideal-gas dimensionless Helmholtz energy:

$$\alpha^\circ(\tau,\delta) = \frac{h_0^\circ \tau}{RT_c} - \frac{s_0^\circ}{R} - 1 + \ln\frac{\delta\tau_0}{\delta_0\tau} - \frac{\tau}{R}\int_{\tau_0}^{\tau}\frac{c_p^\circ}{\tau^2}\mathrm{d}\tau + \frac{1}{R}\int_{\tau_0}^{\tau}\frac{c_p^\circ}{\tau}\mathrm{d}\tau, \qquad (5)$$

where $\tau_0 = T_c/T_0$, $\delta_0 = \rho_0/\rho_c = p_0/(RT_0\rho_c)$, T_0 is the temperature at a reference state, p_0 is a reference pressure for the ideal-gas properties, and ρ_0 is the ideal-gas density at (T_0, p_0). This work initially correlated a c_p° equation by fitting experimental data of Kano et al. [17], and further adjusted it during the fitting of the residual part so that better agreement was obtained with experimental vapor-phase sound speeds. The final c_p° equation has the form

$$\frac{c_p^\circ}{R} = n_0^\circ + \sum_{i=1}^{3} n_i^\circ \left(\frac{m_i^\circ}{T}\right)^2 \frac{\exp(m_i^\circ/T)}{[\exp(m_i^\circ/T)-1]^2}\,, \qquad (6)$$

where the coefficients n_i° and exponents m_i° are given in Table 3. Equation 6 satisfies the requirements from statistical mechanics [18], i.e., for nonlinear polyatomic molecules with nine atoms such as R1234yf, the value of c_p° theoretically goes to $4R$ near zero kelvin and $(4+21)R$ at extremely high temperatures when the effects of anharmonicity are not included. Figure 1 shows calculated c_p° values from Eq. 6 over a wide range of temperature, as well as

the experimental data. The average deviation in the derived data of Kano et al. [17] is 0.22 %; this exceeds the experimental uncertainty given by Kano et al. [17] (by 0.1 %). Because their method and that used here both obtained c_p° from sound speed measurements, the true uncertainty is not known. The data of Hulse et al. [19], which are estimated values, are represented with an average deviation of 1.01 %.

The ideal-gas Helmholtz energy derived from Eqs. 5 and 6 is expressed in the form

$$\alpha^\circ(\tau,\delta) = \ln\delta + n_4^\circ + n_5^\circ\tau + (n_0^\circ - 1)\ln\tau + \sum_{i=1}^{3} n_i^\circ \ln\left[1 - \exp\left(-\frac{m_i^\circ \tau}{T_\mathrm{c}}\right)\right]. \quad (7)$$

The values of n_4° and n_5°, which are also given in Table 3, were determined so that the specific enthalpy and entropy of the saturated liquid state at 0 °C are 200 $\mathrm{kJ \cdot kg^{-1}}$ and 1 $\mathrm{kJ \cdot kg^{-1} \cdot K^{-1}}$, respectively, corresponding to the common convention of the refrigeration industry. The large number of digits given for n_4° and n_5° are required to reproduce these enthalpy and entropy values specified at the reference state.

Table 3 Coefficients and exponents of eqs 6 and 7 for R1234yf.

i	n_i°	m_i°
0	4.0	-
1	8.65	512
2	9.75	1570
3	2.11	4500
4	−12.081525543189	-
5	8.52896238365	-

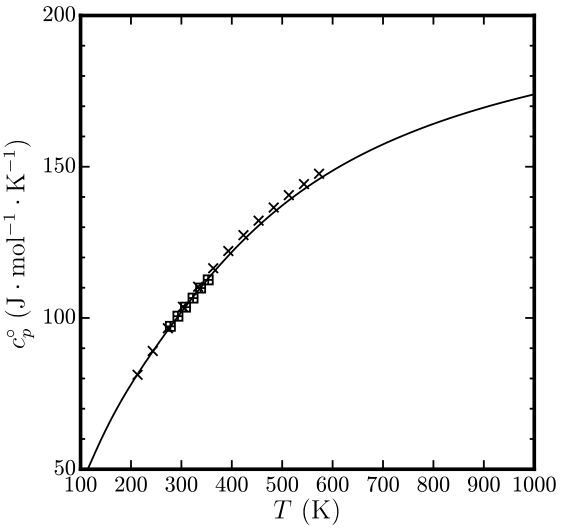

Fig. 1 Ideal-gas isobaric heat capacity (c_p°) of R1234yf: (×) Hulse et al. [19], (⊞) Kano et al. [17], (—) Eq. 6.

4.2 Residual Helmholtz Energy

The residual Helmholtz energy is empirically determined by fitting experimental data. Recent trends in the development of accurate equations of state for industrial fluids often use the functional form:

$$\alpha^{\mathrm{r}}(\tau,\delta) = \sum n_i \tau^{t_i} \delta^{d_i} + \sum n_i \tau^{t_i} \delta^{d_i} \exp(-\delta^{e_i}) + \sum n_i \tau^{t_i} \delta^{d_i} \exp\left[-\eta_i(\delta-\varepsilon_i)^2 - \beta_i(\tau-\gamma_i)^2\right], \tag{8}$$

where the first, second, and final summations are called polynomial, exponential, and Gaussian bell-shaped (simply Gaussian) terms, respectively. The number of terms, coefficients (n_i), exponents (t_i, d_i, and e_i), and other parameters (η_i, ε_i, β_i, and γ_i) are determined through nonlinear least-square fitting. The algorithm for this procedure was originally developed by Lemmon

and Jacobsen [14] and has been greatly extended by collaborations between correlators [11,20–24] over the last decade. The most recent fitting techniques, which were used in this work, are summarized here.

An objective function minimized in the fitting (S) consisted of three sums as follows:

$$S = \psi_1 S_1 + \psi_2 S_2 + \psi_3 S_3, \tag{9}$$

where

$$S_1 = \sum W_i F_i^2, \tag{10}$$

$$S_2 = \sum P_i, \tag{11}$$

and

$$S_3 = \sum L_i. \tag{12}$$

The sums S_1, S_2, and S_3 are the sum of squared relative deviations in experimental data from calculated values (F_i^2), the sum of penalties added to mold the equation to certain thermodynamic constraints (P_i), and the sum of penalties added to keep the coefficients and exponents of the equation within appropriate ranges (L_i); ψ_1, ψ_2, and ψ_3 are their scaling factors. Experimental data for the vapor pressure, density, critical parameters, and sound speed in the vapor and liquid phases were used while fitting, and deviations in selected data points of these properties were added to S_1 with their weighting factors W_i determined according to property type, region, and uncertainty.

Various thermodynamic constraints were considered to ensure that the equation of state was well behaved near the critical point and would reliably

extrapolate beyond the range of the experimental data. Examples of the constraints are given by Akasaka and Lemmon [24]. If the equation violated the i^{th} constraint, then a penalty P_i was added to S_2, where values of P_i depend on how much the constraint was violated.

Adjustable ranges for the coefficients and exponents were limited during fitting. Recent studies [24,25] found the ranges appropriate for equations that exhibit reasonable behavior over wide ranges of temperature and pressure. For example, η_i and β_i were constrained to be within 0.8 to 2.5. If the exponents exceeded the boundaries, then a penalty L_i was added to S_3. Although these limitations are basically empirical, they are necessary to obtain reliable equations.

The scaling factors ψ_1, ψ_2, and ψ_3 were used to change the contributions of S_1, S_2, and S_3 to the objective function S. Larger values were initially given to ψ_2 and ψ_3 rather than ψ_1 to roughly shape the functional form. Once S_2 and S_3 had become sufficiently small, the value of ψ_1 was gradually increased until selected experimental data were properly represented.

The final form of the equation is

$$\begin{aligned}\alpha^{\mathrm{r}}(\tau,\delta) = &\sum_{i=1}^{5} n_i \tau^{t_i} \delta^{d_i} + \sum_{i=6}^{10} n_i \tau^{t_i} \delta^{d_i} \exp(-\delta^{e_i}) \\ &+ \sum_{i=11}^{17} n_i \tau^{t_i} \delta^{d_i} \exp\left[-\eta_i(\delta-\varepsilon_i)^2 - \beta_i(\tau-\gamma_i)^2\right], \end{aligned} \tag{13}$$

where the coefficients and exponents are given in Table 4. The large number of digits for n_3 and n_4 are required to exactly represent the critical point. The terms in Eq. 13 are less intercorrelated than most previously developed equa-

tions, and the functional form can be used in the fits of other refrigerants with slight adjustments of the coefficients and exponents. Akasaka et al. [25] and Akasaka and Lemmon [26] successfully applied this form to the equations for trifluoroethene (R1123) and trans-1,2-difluoroethene [R1132(E)], respectively.

Table 4 Coefficients and exponents of Eq. 13 for R1234yf.

i	n_i	t_i	d_i	e_i	η_i	β_i	γ_i	ε_i
1	0.0340387	1.0	4					
2	1.912859	0.222	1					
3	−2.1984719881617	0.61	1					
4	−0.8147645305033	1.122	2					
5	0.2288282	0.5	3					
6	−1.65436	2.14	1	2				
7	−1.446628	2.284	3	2				
8	0.5961722	1.05	2	1				
9	−0.6148209	2.33	2	2				
10	−0.0180069	0.778	7	1				
11	0.2845275	1.0	1		28.1	1016.0	1.061	0.96
12	−0.3050809	2.0	1		28.0	1000.0	1.062	0.96
13	2.198935	1.236	1		1.307	1.16	1.3	0.853
14	−0.4270329	1.6	1		1.96	1.2	1.04	1.15
15	−0.4015581	1.85	1		1.25	1.26	1.0	1.3
16	0.1179587	0.7	1		1.0	1.6	1.14	1.5
17	−0.3141002	1.75	1		2.2	0.87	1.1	0.762

5 Available Experimental Data and Comparisons to the Equation of State

Table 5 summarizes the experimental data currently available for R1234yf and their average absolute deviations (AADs) in calculated values from the equation of state. The AAD in any property X is defined as

$$\mathrm{AAD}_X = \frac{100}{N_{\mathrm{exp}}} \sum_{i=1}^{N_{\mathrm{exp}}} \left| \frac{X_{i,\,\mathrm{exp}} - X_{i,\,\mathrm{calc}}}{X_{i,\,\mathrm{exp}}} \right|, \tag{14}$$

where N_{exp} is the number of data points in a dataset, $X_{i,\,\mathrm{exp}}$ is the i^{th} experimental value, and $X_{i,\,\mathrm{calc}}$ is the calculated value at the state conditions for $X_{i,\,\mathrm{exp}}$. Figures 2 and 3 show the distributions of available experimental (p, ρ, T) and sound speed data on a p–T diagram, as well as the vapor pressure curve calculated from the equation of state.

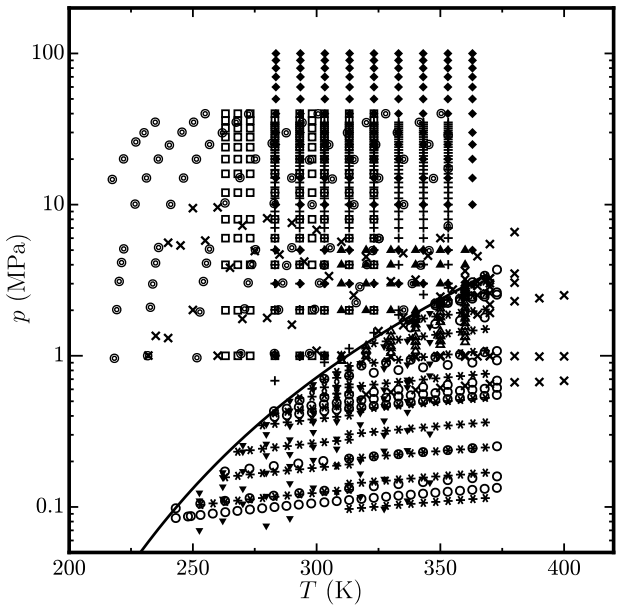

Fig. 2 Distribution of experimental (p, ρ, T) data of R1234yf: (□) Yoshitake et al. [39], (◯) Di Nicola et al. [40], (▲) Tanaka et al. [41], (×) Richter et al. [4], (△) Tanaka and Higashi [42], (+) Fedele et al. [43], (◎) Klomfar et al. [44], (⧫) Qiu et al. [45], (▼) Hu et al. [46], (∗) Yin et al. [38].

5.1 Saturation Properties

For the vapor pressure, 15 datasets are currently available for R1234yf. Figure 4 shows relative deviations (upper panel) and absolute differences (lower panel) in experimental vapor pressures from calculated values with the equation of state. All datasets are generally consistent within 0.3 % at temperatures above 250 K, except the earliest two datasets [19,27], which are sometimes off-scale in this figure. The datasets [19,27] have higher uncertainties than other datasets probably due to their lower purity. If these two datasets are excluded,

Table 5 Experimental data for the thermodynamic properties of R1234yf.

			Purity	Range		AAD
Author	Year	N	(mol%)	T (K)	p (MPa)	(%)
Vapor pressure						
Hulse et al. [19]	2009	12	N/A	241–353		1.37
Kano et al. [27]	2009	10	99	303–367		0.36
Di Nicola et al. [28]	2010	34	99.95	224–363		0.10
Tanaka and Higashi [7]	2010	11	99.99	310–360		0.12
Fedele et al. [29]	2011	40	99.5[a]	246–343		0.13
Richter et al. [4]	2011	30	99.96	250–366		0.06
Hu et al. [30]	2013	5	99.9[a]	283–323		0.24
Kamiaka et al. [31]	2013	7	99	273–333		0.10
Chen et al. [32]	2015	5	99.9[a]	283–323		0.05
Madani et al. [33]	2016	7	99[b]	254–348		0.16
Yang et al. [34]	2016	4	99.9[a]	283–313		0.03
Kochenburger et al. [35]	2017	13	99.5[a]	193–273		0.52
Hu et al. [36]	2018	5	99.9[a]	283–323		0.05
Valtz et al. [37]	2019	27	99.5[b]	276–337		0.14
Yin et al. [38]	2019	24	99.9	253–367		0.09
Saturated liquid density						
Hulse et al. [19]	2009	9	N/A	265–365		0.10
Tanaka and Higashi [7]	2010	10	99.99	348–T_c		0.84
Saturated vapor density						
Tanaka and Higashi [7]	2010	12	99.99	356–T_c		2.75
(p, ρ, T) data						
Yoshitake et al. [39]	2009	115	99.93	263–323	1.00–40.0	0.03
Di Nicola et al. [40]	2010	134	99.95	243–373	0.08–3.72	0.42
Tanaka et al. [41]	2010	23	99.99	310–360	1.00–5.00	0.07
Richter et al. [4]	2011	93	99.96	232–400	0.55–9.59	0.04
Tanaka and Higashi [42]	2011	202	99.95	310–360	0.93–2.89	0.18
Fedele et al. [43]	2012	280	99.5[a]	283–353	0.68–35.0	0.14
Klomfar et al. [44]	2012	89	99.5[a]	217–353	0.68–40.0	0.04
Qiu et al. [45]	2013	128	99.9[a]	283–363	1.00–100	0.17
Hu et al. [46]	2017	83	99.9[a]	253–346	0.07–1.91	0.18
Yin et al. [38]	2019	172	99.9	253–368	0.10–3.37	0.21

Table 5 (continued)

Author	Year	N	Purity (mol%)	Range T (K)	Range p (MPa)	AAD (%)
Isobaric heat capacity						
Tanaka et al. [41]	2010	22	99.99	310–360	2.00–5.00	1.96
Gao et al. [47]	2014	74	99.9[a]	305–355	1.50–5.08	0.31
Liu et al. [48]	2017	154	99.95[a]	304–373	1.51–12.0	2.31
Lukawski et al. [49]	2018	33	99.99[a]	373–413	3.50–10.0	1.84
Kagawa and Matsuguchi [50]	2020	62	99.95[a]	289–353	0.20–2.20	0.58
Sheng et al. [51]	2022	33	99.9	232–284	2.00–7.13	0.32
Isochoric heat capacity						
Zhong et al. [52]	2018	74	99.9	241–340	1.67–12.8	1.46
Speed of sound						
Yoshitake et al. [39]	2009	212	99.93	263–333	0.28–22.1	0.15
Kano et al. [17]	2010	41	99.9	278–353	0.03–0.41	0.01
Lago et al. [53]	2011	22	99.5[a]	260–360	1.99–6.06	0.97
McLinden and Perkins [54]	2022	345	99.94	235–380	0.64–25.8	0.05
Ideal-gas isobaric heat capacity						
Hulse et al. [19]	2009	13	N/A	213–573		1.01
Kano et al. [17]	2010	6	99.9	278–353		0.22

[a]mass%

[b]vol%

the overall averages of relative deviations and absolute differences in all data above 250 K (a total of 196 data points) are 0.090 % and 0.72 kPa. They are similar to typical experimental uncertainties in measurements of the vapor pressure.

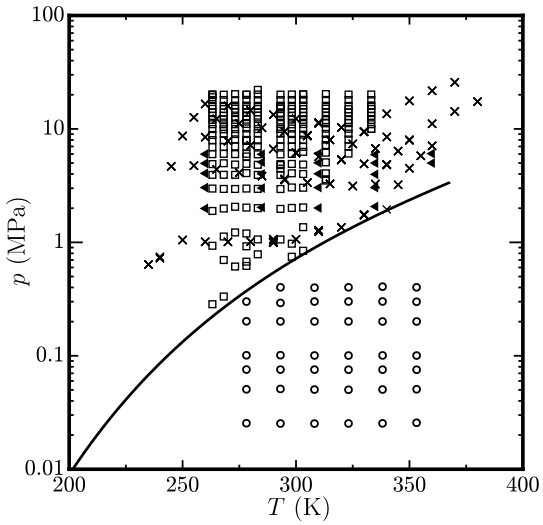

Fig. 3 Distribution of experimental data for the sound speed of R1234yf: (□) Yoshitake et al. [39], (◯) Kano et al. [17], (◀) Lago et al. [53], (×) McLinden and Perkins [54].

The data of Richter et al. [4] and those of Di Nicola et al. [28] show very similar trends, and they are represented within 0.1 % at temperatures from 270 K to the critical temperature. In this range, the maximum difference in both datasets from the equation is about 1 kPa; this is comparable to their experimental uncertainties. At temperatures below 270 K, larger relative deviations up to 0.54 % in the data of Richter et al. [4] and 0.83 % in those of Di Nicola et al. [28] are observed due to the low vapor pressures, but the differences are still less than 1 kPa. The data of Richter et al. [4] and Di Nicola et al. [28] are mostly consistent with those of Fedele et al. [29], Kamiaka et al. [31], Chen et al. [32], Madani et al. [33], Yang et al. [34], Hu et al. [36], and Yin et al. [38], and the equation reproduces these data within their uncertainties. The typical relative deviation in these data is 0.1 %. The data of

Hu et al. [30] show systematic negative deviations down to −0.4 %. The data of Kochenburger et al. [35] are located at four temperatures (193 K, 223 K, 233 K, and 272 K); the data at 272 K are reasonably represented with an average deviation of 0.20 %, but the other data show larger deviations up to 0.5 % due to the low vapor pressures (lower than atmospheric pressure). The data of Valtz et al. [37] show negative deviations at temperatures below 300 K and positive deviations at higher temperatures. The absolute deviation at the highest temperature (336 K) exceeds the experimental uncertainty, but the average deviation (0.14 %) is acceptable.

Experimental data are limited for the saturated liquid and vapor densities, but calculated values for these properties from the equation of state should be reliable due to the accurate and consistent vapor pressure and single-phase (p, ρ, T) data used in the fitting process. Figure 5 depicts the saturation boundary above 340 K obtained from the equation of state on a T–ρ diagram, along with experimental data for saturated liquid and vapor densities. Figure 6 shows relative deviations in the experimental data for saturated liquid densities. The saturated vapor and liquid densities of Tanaka and Higashi [7] were measured during the critical point determination. The equation represents the saturated liquid densities of Tanaka and Higashi [7] with an average deviation of 0.84 %. The average deviation in the saturated vapor densities of Tanaka and Higashi [7] are larger (2.75 %) due to higher experimental uncertainties. The data of Hulse et al. [19] also agree well with the equation; the average deviation is 0.10 %. Figure 5 includes the rectilinear diameter, indicated by the dashed

line, which is almost straight up to the critical point. The saturation boundary and rectilinear diameter over a wider range of temperature and density are shown in Section 6.

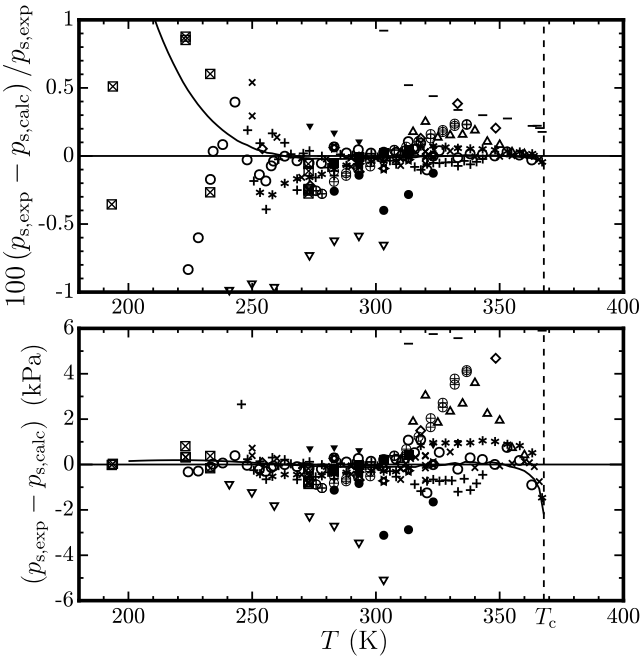

Fig. 4 Relative deviations and differences in experimental vapor pressures from calculated values with the equation of state: (▽) Hulse et al. [19], (−) Kano et al. [27], (◯) Di Nicola et al. [28], (△) Tanaka and Higashi [7], (+) Fedele et al. [29], (×) Richter et al. [4], (•) Hu et al. [30], (▼) Kamiaka et al. [31], (◁) Chen et al. [32], (◊) Madani et al. [33], (■) Yang et al. [34], (⊠) Kochenburger et al. [35], (▷) Hu et al. [36], (⊕) Valtz et al. [37], (∗) Yin et al. [38], (———) Richter et al. [4] (Equation of state).

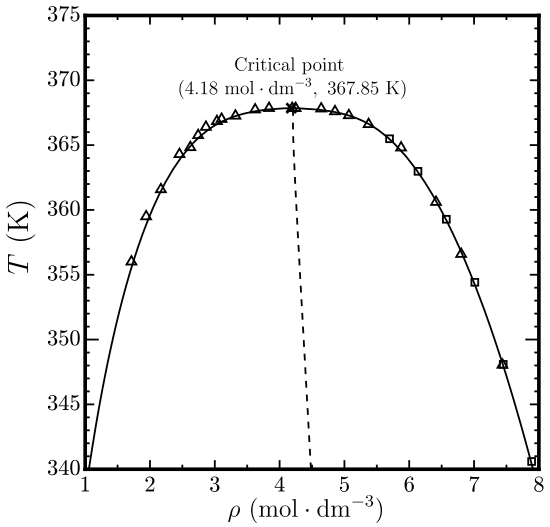

Fig. 5 Saturation boundary near the critical point obtained from the equation of state and experimental data for the saturated liquid and vapor densities: (□) Hulse et al. [19], (△) Tanaka and Higashi [7]. The dashed line shows the rectilinear diameter.

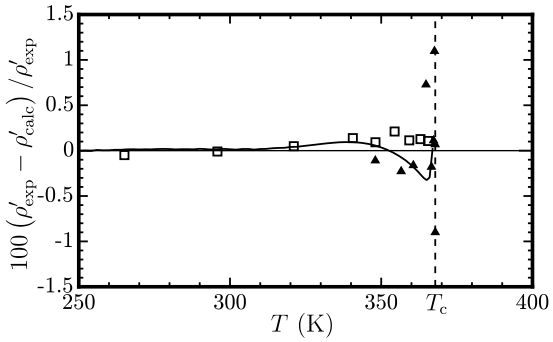

Fig. 6 Relative deviations in experimental data for saturated liquid densities from calculated values with the equation of state: (□) Hulse et al. [19], (▲) Tanaka and Higashi [7], (——) Richter et al. [4] (Equation of state).

5.2 (p, ρ, T) data

For the (p, ρ, T) behavior of R1234yf, ten experimental datasets are currently available. Figure 7 shows relative deviations between the experimental densi-

ties and calculated values from the equation of state in different temperature intervals. There are 674 data points for the liquid phase, and their overall average deviation is 0.11 % in density. For the vapor phase and supercritical regions, 645 data points are shown, and their overall average deviation is 0.23 %. Data near the critical point sometimes show larger deviations up to 1 %.

The data of Richter et al. [4] include densities both for the liquid and vapor phases, and cover wide ranges of temperature and pressure with very low uncertainties. The equation represents the data with an average deviation of 0.04 %; this is comparable to the experimental uncertainties. The liquid phase data of Richter et al. [4] show good consistency with those of Yoshitake et al. [39], Tanaka et al. [41], and Klomfar et al. [44], and these data are represented with average deviations less than 0.1 %. The data of Fedele et al. [43] show systematic negative deviations down to −0.45 %, but 93 % of the data points show deviations less than 0.2 %. The data of Qiu et al. [45] are more scattered and less consistent with the other liquid-phase data. At the highest pressure (100 MPa), deviations are 0.20–0.25 %. For the vapor phase, the data of Tanaka and Higashi [42] and Hu et al. [46] are represented mostly within 0.5 %. Their average deviations are both 0.18 %, which is less than general experimental uncertainties in measurements of vapor densities. The data of Di Nicola et al. [40] and Yin et al. [38] are more scattered and show larger deviations. Systematic positive deviations are observed in the data of Di Nicola et al. [40]. Deviations in the data of Yin et al. [38] are within 0.2 %

at pressures below 1 MPa, but they become larger (down to −1 %) at higher pressures.

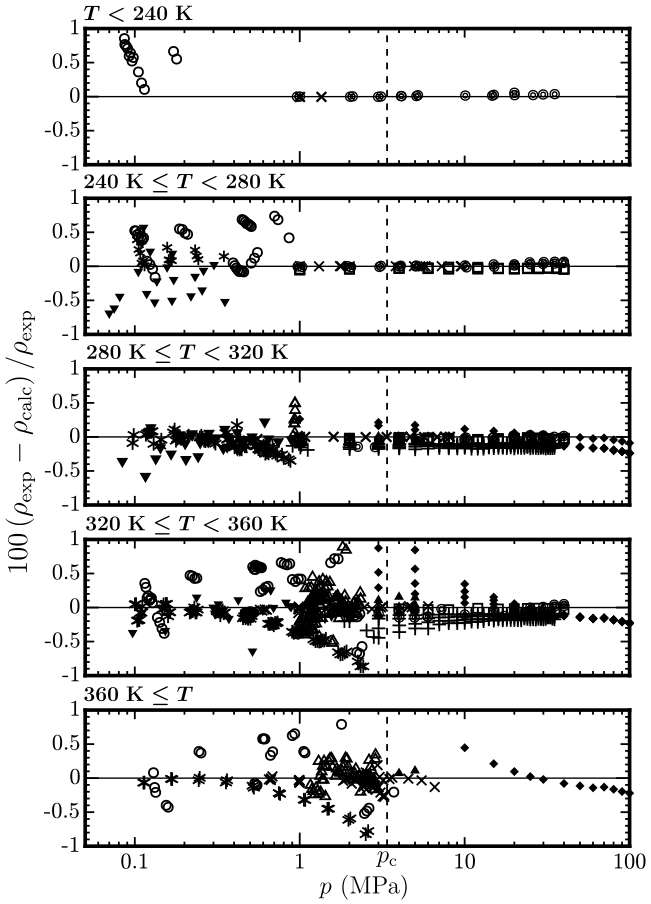

Fig. 7 Relative deviations in experimental densities from calculated values with the equation of state: (□) Yoshitake et al. [39], (◯) Di Nicola et al. [40], (▲) Tanaka et al. [41], (×) Richter et al. [4], (△) Tanaka and Higashi [42], (+) Fedele et al. [43], (◎) Klomfar et al. [44], (♦) Qiu et al. [45], (▼) Hu et al. [46], (∗) Yin et al. [38]. The vertical dashed line indicates the critical pressure.

5.3 Caloric Data

Four datasets are available for the sound speed of R1234yf; one for the vapor phase and the rest for the liquid phase. Deviations in these data are shown in Fig. 8. The data of Kano et al. [17] for the vapor phase are accurately represented; the maximum and average deviations are 0.027 % and 0.010 %, respectively. Inconsistency is observed among the three datasets for the liquid phase. Overall, the data of McLinden and Perkins [54] are represented with an average deviation of 0.05 %. The data of Yoshitake et al. [39] show systematic negative deviations down to −0.36 %, but their average deviation (0.15 %) is acceptable. The data of Lago et al. [53] are quite different from the other two datasets. The deviations are still acceptable at 260 K, but they become considerably larger (up to 2.5 %) at higher temperatures. The data at the highest temperature (360 K) are off-scale.

For the isobaric heat capacity, six datasets are currently available. The data of Kagawa and Matsuguchi [50] are located in the vapor phase, and those of Tanaka et al. [41], Gao et al. [47], Liu et al. [48], and Sheng et al. [51] are liquid phase. The data of Lukawski et al. [49] are located in the supercritical region. Some supercritical region data are also included in the dataset of Liu et al. [48]. The only dataset is that of Zhong et al. [52] for the isochoric heat capacity.

Figure 9 shows deviations in the isobaric heat capacity data and Fig. 10 plots three isotherms in the supercritical region on a c_p-T diagram, as well as the data of Liu et al. [48] and Lukawski et al. [49]. A total of 378 data points

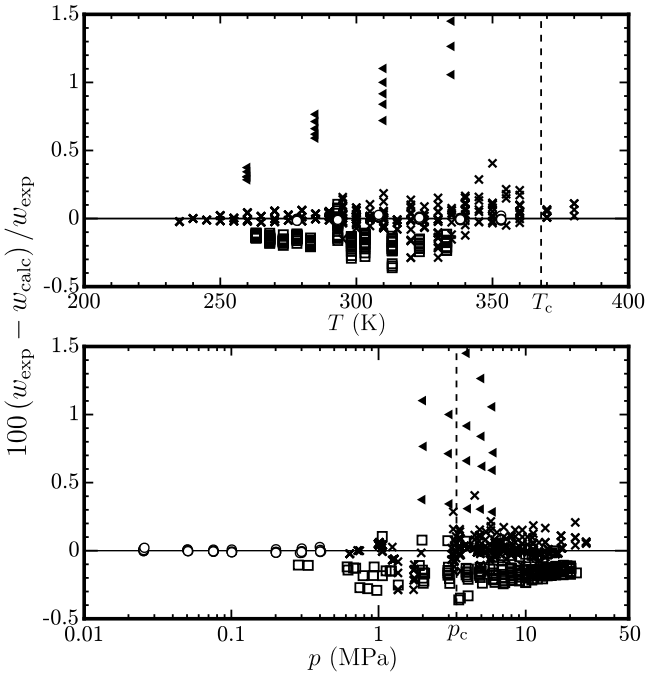

Fig. 8 Relative deviations in experimental data for sound speed from calculated values with the equation of state: (□) Yoshitake et al. [39], (○) Kano et al. [17], (◀) Lago et al. [53], (×) McLinden and Perkins [54].

are shown in Fig. 9, and their overall average deviation is 1.40 %. This is comparable with general experimental uncertainties in measurements for heat capacities. Overall, systematic deviations are not observed, except in the data of Liu et al. [48]. The vapor-phase data of Kagawa and Matsuguchi [50] are well represented with an average deviation of 0.58 %, which is within the experimental uncertainties. This indicates that the data of Kano et al. [17] for the vapor-phase sound speed and ideal-gas isobaric heat capacity are consistent with the isobaric heat capacities of Kagawa and Matsuguchi [50]. The data of Gao et al. [47] for the liquid phase are also well represented. The average

deviation is 0.31 %, and is considerably smaller than their overall experimental uncertainty (1.7 %). For the liquid phase, good consistency is also observed between the data of McLinden and Perkins [54] for the sound speed and those of Gao et al. [47] for the isobaric heat capacity. The data of Tanaka et al. [41] have larger experimental uncertainties (5 %) than the other datasets. Deviations in all data points of the data of Tanaka et al. [41] are within this uncertainty. The data of Liu et al. [48] are slightly inconsistent with the other liquid-phase data; systematic negative deviations down to −5.4 % are observed in the data. The data of Lukawski et al. [49] for the supercritical region show good agreement with the equation of state, as confirmed in Fig. 10; the average deviation in the data is 1.84 %, which is similar to the experimental uncertainties. Deviations in the experimental isochoric heat capacities of Zhong et al. [52] are shown in Fig. 11. The data at temperatures around 270 K show good agreement, and at higher temperatures systematic positive deviations up to 2.4 % are observed. Conversely, deviations at lower temperatures are systematically negative. The average deviation is 1.46 %, which is somewhat larger than their experimental uncertainties (0.8–1.0 %) but acceptable.

6 Extrapolation Behavior of the Equation of State

In order to verify the behavior of the new equation of state in regions away from the available experimental data, various plots of constant-property lines on several thermodynamic coordinates are shown.

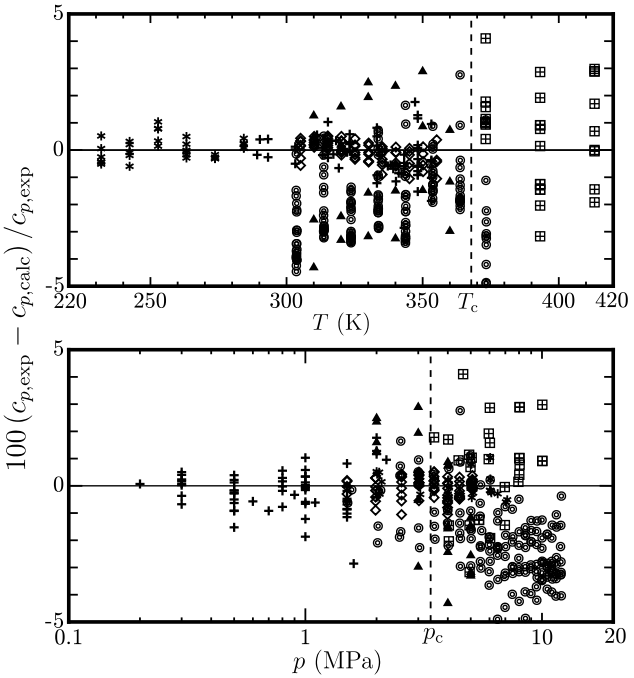

Fig. 9 Relative deviations in experimental data for the isobaric heat capacity from calculated values with the equation of state: (▲) Tanaka et al. [41], (◊) Gao et al. [47], (◎) Liu et al. [48], (⊞) Lukawski et al. [49], (+) Kagawa and Matsuguchi [50], (∗) Sheng et al. [51].

Figure 12 shows values of $(Z-1)/\rho$ calculated from the equation of state along isotherms in the vapor phase. When these values are plotted versus density, the y intercept (zero density) of each isotherm is equal to the second virial coefficient at the given temperature, and the slope at zero density is equal to the third virial coefficient. All isotherms are very smooth, and no physically incorrect behavior is observed. Figure 13 shows plots of the second, third, and fourth virial coefficients (B, C, and D) calculated from the equation of state over a wide temperature range. Based on the analysis of an equation of state for the Lennard-Jones fluid, Thol et al. [55] described the expected behavior

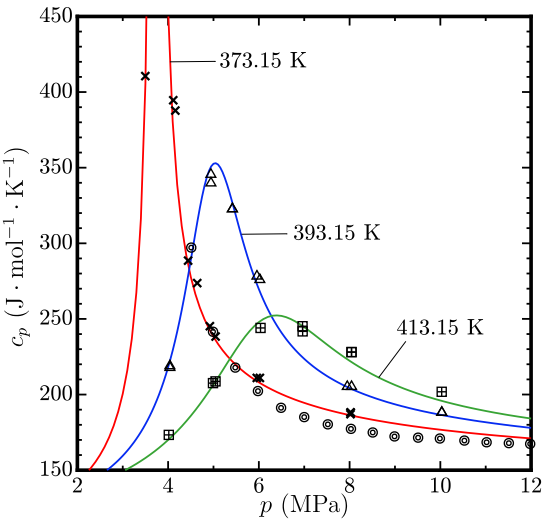

Fig. 10 Isobaric heat capacity calculated from the equation of state and experimental data in the supercritical region: (◎) Liu et al. [48] (373.15 K), (×) Lukawski et al. [49] (373.15 K), (△) Lukawski et al. [49] (393.15 K), (⊞) Lukawski et al. [49] (413.15 K).

of the virial coefficients; that is, B and C should go to negative infinity at zero temperature, pass though zero at a moderate temperature, increase to a maximum, and then approach zero at extremely high temperatures. The theoretical trend in D is slightly different from those of B and C at temperatures higher than the first maximum; there should be a second maximum that is smaller in magnitude than the first maximum, and then D should decrease to zero at very high temperatures. The observed behavior in Fig. 13 is in accord with the expected behavior.

Figures 14 and 15 show the isochoric heat capacity c_v and isobaric heat capacity c_p versus temperature at various pressures from zero to very high values. These figures illustrate that the behavior of the equation is quite appropriate within the range of validity, and that the extrapolation is also reasonable at

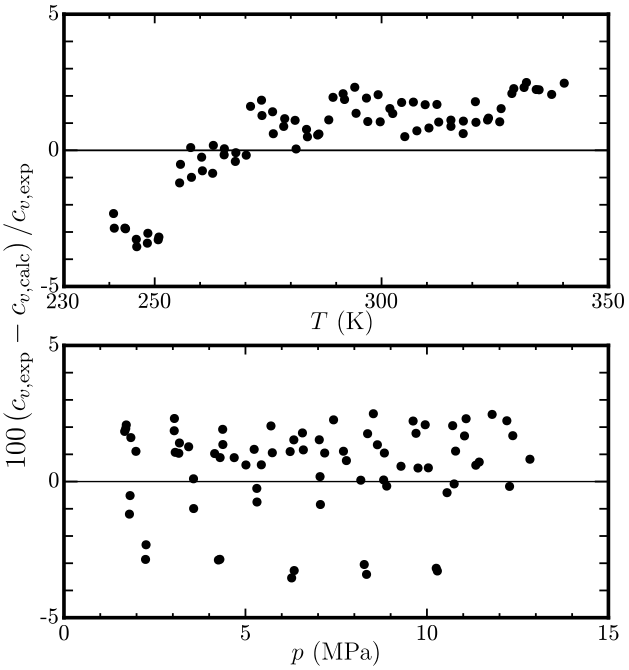

Fig. 11 Relative deviations in experimental data for the isochoric heat capacity from calculated values with the equation of state: (•) Zhong et al. [52].

higher temperatures and pressures, and at lower temperatures below the triple point temperature (121.6 K). An upward trend is observed in the liquid region at low temperatures. This is common among accurate equations and has been validated experimentally for many fluids. In Fig. 16, sound speeds calculated from the equation are plotted versus temperature. The saturated liquid line in this figure is a smooth arc, which is physically correct when depicted on a logarithmic temperature scale.

Figure 17 shows the density behavior along isobars. All isobars are very smooth and do not cross at pressures from 0.1 to 1000 MPa. The rectilinear diameter is straight as it approaches the critical point, giving further validation

to saturated vapor densities calculated from the equation of state. Figure 18 indicates that the extrapolation behavior of isotherms at extremely high temperatures, pressures, and densities is reasonable. The isotherms do not cross even at extreme conditions. As explained by Lemmon and Jacobsen [14], the smooth behavior at extreme conditions comes from the term with $t_i = 1$ and $d_i = 4$ (the term with the largest value of d_i in the polynomial terms).

The phase identification parameter (PIP) [56], which is used to distinguish the vapor or liquid phase condition of any state, was examined to reveal any possible underlying problems in the equation of state. The PIP is defined as

$$\mathrm{PIP} = 2 - \rho \left[\frac{\dfrac{\partial^2 p}{\partial \rho \partial T}}{\left(\dfrac{\partial p}{\partial T}\right)_\rho} - \frac{\left(\dfrac{\partial^2 p}{\partial \rho^2}\right)_T}{\left(\dfrac{\partial p}{\partial \rho}\right)_T} \right]. \tag{15}$$

If the PIP at any given condition is greater than 1, the state is in the liquid phase. If the PIP is less than 1, the state is in the vapor phase. Figure 19 shows the PIP versus temperature along isobars from 0.1 to 1000 MPa, and Fig. 20 displays the PIP versus density along isotherms from 100 to 5000 K. The isobars, isotherms, and saturation lines in these figures are smooth over wide ranges of temperature and density, and no unrealistic behavior is observed.

In Fig. 21, four characteristic curves obtained from the equation are plotted on a p–T diagram. Their definitions are given in Table 6. These curves are very useful in assessing the behavior in regions without available experimental data. As shown in this figure, the reasonable shapes of these curves indicate qualitatively correct extrapolation behavior of the equation extending to extremely high pressures and temperatures.

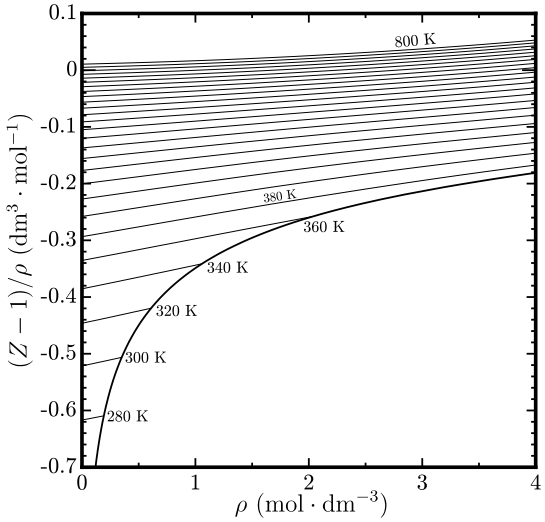

Fig. 12 Values of $(Z-1)/\rho$ calculated from the equation of state along isotherms in the vapor phase. Isotherms are shown between 280 K and 800 K in intervals of 20 K.

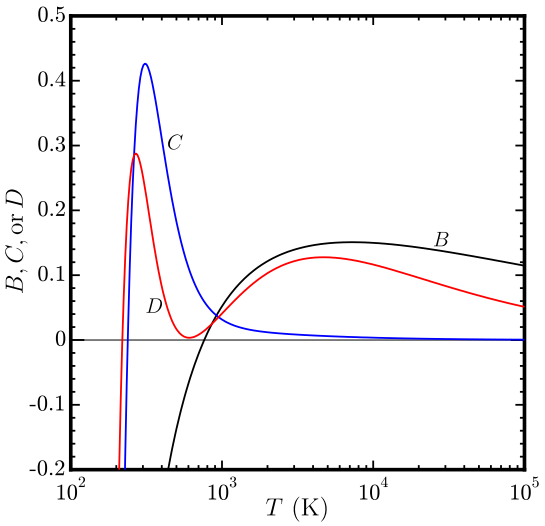

Fig. 13 Second, third, and fourth virial coefficients, B, C, and D, versus temperature. In this plot, the values along the y-axis are equal to the value of B, the value of $10\,C$, and the value of $100\,D$. The units of B, C, and D are dm$^3\cdot$mol^{-1}, dm$^6\cdot$mol^{-2}, and dm$^9\cdot$mol^{-3}, respectively.

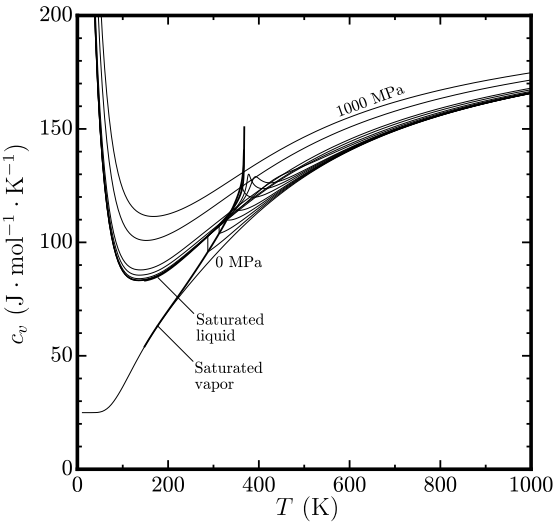

Fig. 14 Isochoric heat capacity c_v versus temperature diagram. Isobars are shown at pressures of 0 (ideal gas), 0.5, 1, 1.5, 2, 3, 4, 5, 10, 20, 50, 100, 500, and 1000 MPa.

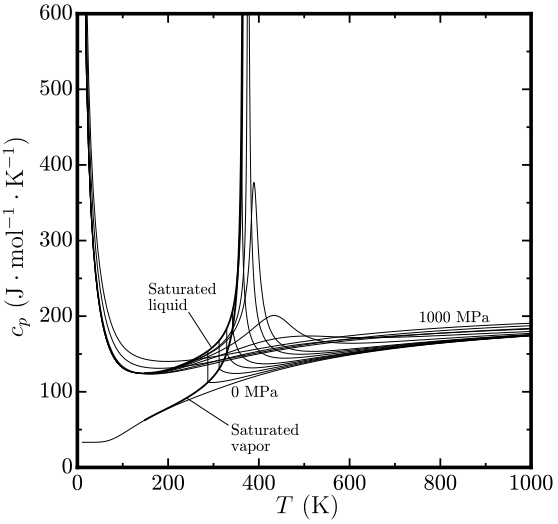

Fig. 15 Isobaric heat capacity c_p versus temperature diagram. Isobars are shown at pressures of 0 (ideal gas), 0.5, 1, 1.5, 2, 3, 4, 5, 10, 20, 50, 100, 500, and 1000 MPa.

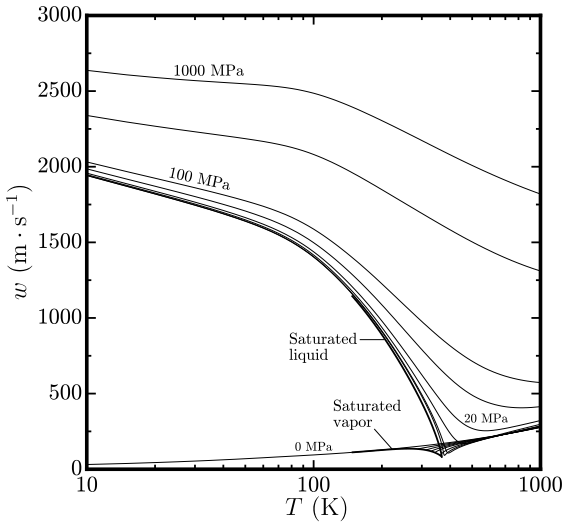

Fig. 16 Sound speed w versus temperature diagram. Isobars are shown at pressures of 0 (ideal gas), 0.5, 1, 1.5, 2, 3, 4, 5, 10, 20, 50, 100, 500, and 1000 MPa.

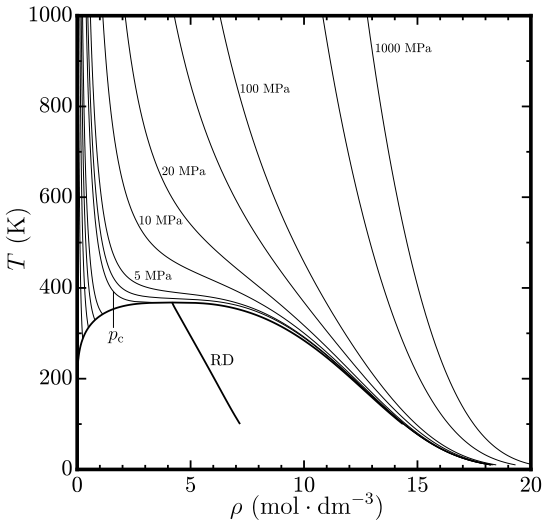

Fig. 17 Isobaric behavior of the equation of state. Isobars are shown at pressures of 0.1, 0.5, 1, 1.5, 2, p_c, 4, 5, 10, 20, 50, 100, 500, and 1000 MPa. RD: Rectilinear diameter.

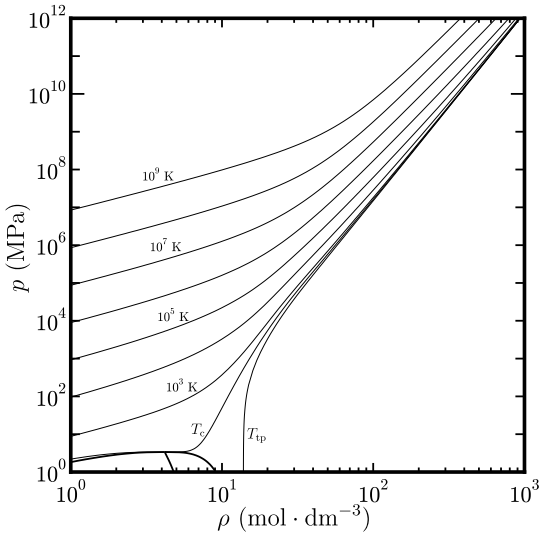

Fig. 18 Isothermal behavior of the equation of state. Isotherms are shown at temperatures of $T_{\rm tp}$, $T_{\rm c}$, 10^3, 10^4, 10^5, 10^6, 10^7, 10^8, and 10^9 K.

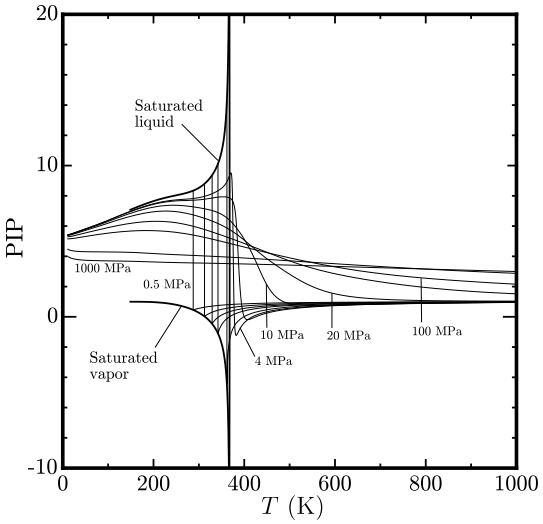

Fig. 19 Phase identification parameter (PIP) versus temperature along isobars at 0.5, 1, 1.5, 2, 3, 4, 5, 10, 20, 50, 100, 500, and 1000 MPa.

Table 6 Four characteristic curves.

Designation	Definition
Ideal curve	$Z = 1$
Boyle curve	$\left(\frac{\partial Z}{\partial \rho}\right)_T = 0$
Joule-Thomson inversion curve	$\left(\frac{\partial Z}{\partial T}\right)_p = 0$
Joule inversion curve	$\left(\frac{\partial Z}{\partial T}\right)_\rho = 0$

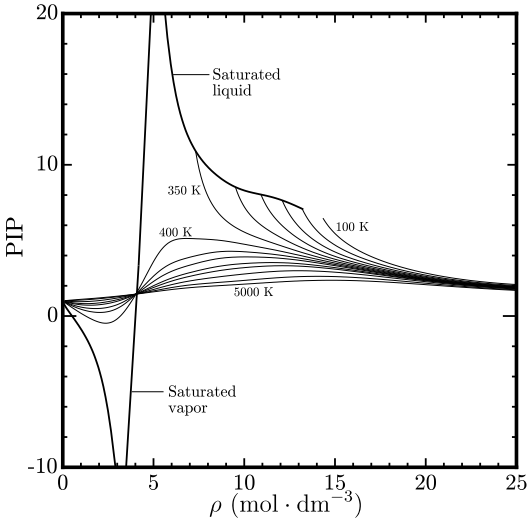

Fig. 20 Phase identification parameter (PIP) versus density along isotherms at 100, 150, 200, 250, 300, 350, 400, 450, 500, 600, 700, 1000, 2000, and 5000 K.

7 Conclusions: Estimated Uncertainties of Calculated Properties

The equation of state developed in this work is valid from the triple point temperature (121.6 K) to 410 K at pressures up to 100 MPa. This equation was based on experimental data for the vapor pressure, (p, ρ, T) data including those at saturation, sound speeds in the vapor and liquid phases, and ideal-gas isobaric heat capacities. The uncertainties presented here are expanded uncer-

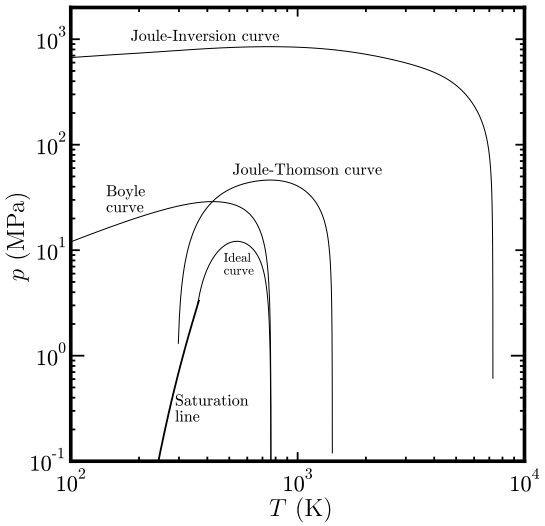

Fig. 21 Four characteristic curves plotted on a pressure-temperature diagram.

tainties ($k = 2$) based on the statistical analysis of deviations between reliable experimental data and calculated values from the equation of state. Estimated uncertainties in vapor pressure are 0.1 % at temperatures above 270 K and 0.3 % at lower temperatures. At very low temperatures around 200 K, uncertainties may be larger than 0.5 %, but differences between experimental and calculated values are less than 1 kPa in most cases. The uncertainties in the liquid and vapor densities are 0.1 % and 0.2 %, respectively, at pressures below 40 MPa. At higher pressures, the uncertainties slowly increase up to a maximum of 0.25 % at 100 MPa. The uncertainties in the sound speeds are 0.02 % for the vapor phase and 0.05 % for the liquid phase. The uncertainties in the isobaric heat capacities are 1 % for the vapor phase and 2 % for the liquid phase. The isochoric heat capacities in the liquid phase are reproduced with an uncertainty of 2 %. Various plots of constant-property lines demonstrate

that not only does the equation exhibit correct behavior over all temperatures and pressures within the range of validity, but also that it shows reasonable extrapolation behavior at extremely low and high temperatures, and at high pressures.

Ancillary equations for vapor pressure and saturation densities have been developed that can be employed for fast approximate calculations of the saturation properties or as the initial values for iteration with the equation of state. As an aid in computer implementation, calculated property values from the equation of state are given in Table 7. Supporting Information provides a fluid file (R1234YF.FLD) for use in REFPROP [57] and TREND [58], a fluid file (R1234yf.json) for use in CoolProp [59], and Python code (R1234yf.py) to display the values in Table 7.

The equation of state is the best currently available property representation for R1234yf, and it has been adopted as an international standard by the working group, which recently revised ISO/DIS 17584 [6].

Acknowledgements The authors thank the members of ISO/TC 86/SC 8/WG 7 for their valuable feedback. The authors appreciate Mark O. McLinden, National Institute of Standards and Technology, Boulder, for his assistance during the documentation of this paper, and Ian H. Bell, National Institute of Standards and Technology, Boulder, for his generous support in programming the supplementary computer codes.

References

1. G. Myhre, D. Shindell, F.M. Bréon, W. Collins, J. Fuglestvedt, J. Huang, D. Koch, J.F. Lamarque, D. Lee, B. Mendoza, T. Nakajima, A. Robock, G. Stephens, T. Takemura,

Table 7 Calculated property values from the equation of state for R1234yf to verify computer code.

T	ρ	p	c_v	c_p	w
(K)	$(\mathrm{mol \cdot dm^{-3}})$	(MPa)	$(\mathrm{J{\cdot}mol^{-1}{\cdot}K^{-1}})$	$(\mathrm{J{\cdot}mol^{-1}{\cdot}K^{-1}})$	$(\mathrm{m{\cdot}s^{-1}})$
280	0	0	89.2037	97.5182	149.388
280	11	28.95760	101.930	139.307	738.905
280	0.1	0.2185345	91.3497	102.623	141.882
340	8	2.309798	113.805	195.748	265.888
340	1	1.855076	113.479	168.646	114.354
368	4.2	3.394716	149.703	48981.3	76.3597

H. Zhang, *Anthropogenic and Natural Radiative Forcing. In: Climate Change 2013: The Physical Science Basis. Contribution of Working Group I to the Fifth Assessment Report of the Intergovernmental Panel on Climate Change* (Cambridge University Press, Cambridge, United Kingdom and New York, NY, USA, 2013)

2. O. Nielsen, M. Javadi, M. Sulbaek Andersen, M. Hurley, T. Wallington, R. Singh, Chem. Phys. Lett. **439**(1-3), 18 (2007). DOI 10.1016/j.cplett.2007.03.053
3. ANSI/ASHRAE Standard 34-2019; Designation and Safety Classification of Refrigerants (2019)
4. M. Richter, M.O. McLinden, E.W. Lemmon, J. Chem. Eng. Data **56**(7), 3254 (2011). DOI 10.1021/je200369m
5. R. Akasaka, Int. J. Thermophys. **32**(6), 1125 (2011). DOI 10.1007/s10765-011-0992-0
6. International Organization for Standardization, ISO/DIS 17584 Refrigerant Properties (2022)
7. K. Tanaka, Y. Higashi, Int. J. Refrig. **33**(3), 474 (2010). DOI 10.1016/j.ijrefrig.2009.10.003
8. G. Di Nicola, C. Brandoni, C. Di Nicola, G. Giuliani, J. Therm. Anal. Calorim. **108**(2), 627 (2012). DOI 10.1007/s10973-011-1944-4

9. S. Tomassetti, G. Di Nicola, C. Kondou, Int. J. Refrig. **133**, 172 (2022). DOI 10.1016/j.ijrefrig.2016.02.003
10. E.W. Lemmon, A.R.H. Goodwin, J. Phys. Chem. Ref. Data **29**(1), 1 (2000). DOI 10.1063/1.556054
11. K. Gao, J. Wu, P. Zhang, E.W. Lemmon, J. Chem. Eng. Data **61**(8), 2859 (2016). DOI 10.1021/acs.jced.6b00195
12. CODATA. CODATA Internationally Recommended 2018 Values of the Fundamental Physical Constants (2020). `https://physics.nist.gov/cuu/Constants/` (accessed at October 26, 2020)
13. R. Span, *Multiparameter Equations of State: An Accurate Source of Thermodynamic Property Data* (Springer Berlin, 2000)
14. E.W. Lemmon, R.T. Jacobsen, J. Phys. Chem. Ref. Data **34**(1), 69 (2005). DOI 10.1063/1.1797813
15. H.J. Kretzschmar, T. Zschunke, J. Klinger, A.I. Dittman, *An Alternative Method for the Numerical Calculation of the Maxwell Criterion in Vapour Pressure Computations, Properties of Water And Steam: Proceedings of The 11th International Conference* (CRC Press, 1990)
16. R. Akasaka, J. Therm. Sci. Technol. **3**(3), 442 (2008). DOI 10.1299/jtst.3.442
17. Y. Kano, Y. Kayukawa, K. Fujii, H. Sato, Int. J. Thermophys. **31**(11-12), 2051 (2010). DOI 10.1007/s10765-010-0885-7
18. D.A. McQuarrie, *Statistical Mechanics, CHAPTER 8* (Harper & Row, 1975)
19. R. Hulse, R. Singh, H. Pham, in *Proc. 3rd IIR Conf. Thermophys. Prop. Transf. Process. Refrig.* (Boulder, CO, USA, 2009)
20. E.W. Lemmon, M.O. McLinden, W. Wagner, J. Chem. Eng. Data **54**(12), 3141 (2009). DOI 10.1063/1.556054
21. M. Thol, E.W. Lemmon, R. Span, High Temp.-High Press. **41**(2), 81 (2012)
22. R. Akasaka, Y. Zhou, E.W. Lemmon, J. Phys. Chem. Ref. Data **44**(5), 013104 (2015). DOI 10.1063/1.4913493
23. S. Herrig, M. Thol, A.H. Harvey, E.W. Lemmon, J. Phys. Chem. Ref. Data **47**(5), 043102 (2018). DOI 10.1063/1.5053993

24. R. Akasaka, E.W. Lemmon, J. Chem. Eng. Data **64**(11), 4679 (2019). DOI 10.1021/acs.jced.9b00007

25. R. Akasaka, Y. Higashi, N. Sakoda, S. Fukuda, E.W. Lemmon, Int. J. Refrig. **119**(11), 457 (2020). DOI 10.1016/j.ijrefrig.2020.07.011

26. R. Akasaka, E.W. Lemmon, in *2nd IIR Conference on HFOs and Low GWP Blends* (Osaka, Japan, 2021)

27. Y. Kano, Y. Kayukawa, K. Fujii, in *Proc. 19th Symp. Environ. Eng.* (Naha, Japan, 2009)

28. G. Di Nicola, F. Polonara, G. Santori, J. Chem. Eng. Data **55**(1), 201 (2010). DOI 10.1021/je900306v

29. L. Fedele, S. Bobbo, F. Groppo, J.S. Brown, C. Zilio, J. Chem. Eng. Data **56**(5), 2608 (2011). DOI 10.1021/je2000952

30. P. Hu, L.X. Chen, Z.S. Chen, Fluid Phase Equilib. **360**, 293 (2013). DOI 10.1016/j.fluid.2013.09.056

31. T. Kamiaka, C. Dang, E. Hihara, Int. J. Refrig. **36**(3), 965 (2013). DOI 10.1016/j.ijrefrig.2012.08.016

32. L.X. Chen, P. Hu, W.B. Zhu, L. Jia, Z.S. Chen, Fluid Phase Equilib. **392**, 19 (2015). DOI 10.1016/j.fluid.2015.02.014

33. H. Madani, A. Valtz, F. Zhang, J. El Abbadi, C. Houriez, P. Paricaud, C. Coquelet, Fluid Phase Equilib. **415**, 158 (2016). DOI 10.1016/j.fluid.2016.02.005

34. Z.Q. Yang, L.G. Kou, S. Han, C. Li, Z.J. Hao, W. Mao, W. Zhang, J. Lu, Fluid Phase Equilib. **427**, 390 (2016). DOI 10.1016/j.fluid.2016.07.031

35. T. Kochenburger, D. Gomse, I. Tratschitt, A. Zimmermann, S. Grohmann, Fluid Phase Equilib. **450**, 13 (2017). DOI 10.1016/j.fluid.2017.07.002

36. P. Hu, N. Zhang, L.X. Chen, X.D. Cai, J. Chem. Eng. Data **63**(5), 1507 (2018). DOI 10.1021/acs.jced.7b01073

37. A. Valtz, J.E. Abbadi, C. Coquelet, C. Houriez, Int. J. Refrig. **107**, 315 (2019). DOI 10.1016/j.ijrefrig.2019.07.024

38. J. Yin, G. Zhao, S. Ma, Int. J. Refrig. **107**, 183 (2019). DOI 10.1016/j.ijrefrig.2019.08.008

39. M. Yoshitake, S. Matsuo, T. Sotani, in *Proc. 30th Japan Symp. Thermophys. Prop.* (Yonezawa, Japan, 2009), pp. 353–355 (in Japanese)

40. C. Di Nicola, G. Di Nicola, M. Pacetti, F. Polonara, G. Santori, J. Chem. Eng. Data **55**(9), 3302 (2010). DOI 10.1021/je100102q

41. K. Tanaka, Y. Higashi, R. Akasaka, J. Chem. Eng. Data **55**(2), 901 (2010). DOI 10.1021/je900515a

42. K. Tanaka, Y. Higashi, Trans. Japan Soc. Refrig. Air Cond. Eng. **28**(1), 51 (2011). DOI 10.11322/tjsrae.28.51

43. L. Fedele, J.S. Brown, L. Colla, A. Ferron, S. Bobbo, C. Zilio, J. Chem. Eng. Data **57**(2), 482 (2012). DOI 10.1021/je201030g

44. J. Klomfar, M. Součková, J. Pátek, J. Chem. Eng. Data **57**(11), 3283 (2012). DOI 10.1021/je3009304

45. G. Qiu, X. Meng, J. Wu, J. Chem. Thermodyn. **60**, 150 (2013). DOI 10.1016/j.jct.2013.01.006

46. P. Hu, X.D. Cai, L.X. Chen, H. Xu, G. Zhao, J. Chem. Eng. Data **62**(10), 3353 (2017). DOI 10.1021/acs.jced.7b00427

47. N. Gao, Y. Jiang, J. Wu, Y. He, G. Chen, Fluid Phase Equilib. **376**, 64 (2014). DOI 10.1016/j.fluid.2014.05.029

48. Y. Liu, X. Zhao, S. Lv, H. He, J. Chem. Eng. Data **62**(3), 1119 (2017). DOI 10.1021/acs.jced.6b00959

49. M.Z. Lukawski, M.P. Ishmael, J.W. Tester, J. Chem. Eng. Data **63**(2), 463 (2018). DOI 10.1021/acs.jced.7b00946

50. N. Kagawa, A. Matsuguchi, J. Chem. Eng. Data **65**(9), 4299 (2020). DOI 10.1021/acs.jced.0c00243

51. B. Sheng, Y. Zhao, X. Dong, H. Guo, M. Gong, J. Chem. Thermodyn. **164**, 106626 (2022). DOI 10.1016/j.jct.2021.106626

52. Q. Zhong, X. Dong, Y. Zhao, J. Wang, H. Zhang, H. Li, H. Guo, J. Shen, M. Gong, J. Chem. Thermodyn. **125**, 86 (2018). DOI 10.1016/j.jct.2018.05.022

53. S. Lago, P.A. Giuliano Albo, S. Brignolo, J. Chem. Eng. Data **56**(1), 161 (2011). DOI 10.1021/je100896n

54. M.O. McLinden, R.A. Perkins, submitted to J. Chem. Thermodyn. (2022)

55. M. Thol, G. Rutkai, A. Köster, R. Lustig, R. Span, J. Vrabec, J. Phys. Chem. Ref. Data **45**(2) (2016). DOI 10.1063/1.4945000

56. G. Venkatarathnam, L.R. Oellrich, Fluid Phase Equilib. **301**(4), 225 (2011). DOI 10.1016/j.fluid.2010.12.001

57. E.W. Lemmon, I.H. Bell, M.L. Huber, M.O. McLinden. NIST Standard Reference Database 23: Reference Fluid Thermodynamic and Transport Properties-REFPROP, Version 10.0, National Institute of Standards and Technology (2018). DOI 10.18434/T4JS3C. URL `https://www.nist.gov/srd/refprop`

58. R. Span, R. Beckmüller, S. Hielscher, A. Jäger, E. Mickoleit, T. Neumann, S. Pohl, B. Semrau, M. Thol. TREND. Thermodynamic Reference and Engineering Data 5.0. Lehrstuhl für Thermodynamik, Ruhr-Universität Bochum. (2020)

59. I.H. Bell, J. Wronski, S. Quoilin, V. Lemort, Ind. Eng. Chem. Res. **53**(6), 2498 (2014). DOI 10.1021/ie4033999